

# THE ISOTHERMAL OUTFLOW IN THE MASSIVE STAR-FORMING REGION G240.31+0.07

JUNHAO LIU (刘峻豪),<sup>1</sup> KEPING QIU,<sup>1,2</sup> FRIEDRICH WYROWSKI,<sup>3</sup> KARL MENTEN,<sup>3</sup> ROLF GÜSTEN,<sup>3</sup> YUE CAO,<sup>1</sup> AND YUWEI WANG<sup>1</sup>

<sup>1</sup>*School of Astronomy and Space Science, Nanjing University, 163 Xianlin Avenue, Nanjing 210023, P.R.China*

<sup>2</sup>*Key Laboratory of Modern Astronomy and Astrophysics (Nanjing University), Ministry of Education, Nanjing 210023, P.R.China*

<sup>3</sup>*Max-Planck-Institut für Radioastronomie, Auf dem Hügel 69, 53121 Bonn, Germany*

## ABSTRACT

We present Atacama Pathfinder Experiment (APEX) observations toward the massive star-forming region G240.31+0.07 in the CO J = 3–2, 6–5, and 7–6 lines. We detect a parsec-sized, bipolar, and high velocity outflow in all the lines, which allow us, in combination with the existing CO J = 2–1 data, to perform a multi-line analysis of physical conditions of the outflowing gas. The CO 7–6/6–5, 6–5/3–2, and 6–5/2–1 ratios are found to be nearly constant over a velocity range of  $\sim 5\text{--}25\text{ km s}^{-1}$  for both blueshifted and redshifted lobes. We carry out rotation diagram and large velocity gradient (LVG) calculations of the four lines, and find that the outflow is approximately isothermal with a gas temperature of  $\sim 50\text{ K}$ , and that the CO column density clearly decreases with the outflow velocity. If the CO abundance and the velocity gradient do not vary much, the decreasing CO column density indicates a decline in the outflow gas density with velocity. By comparing with theoretical models of outflow driving mechanisms, our observations and calculations suggest that the massive outflow in G240.31+0.07 is being driven by a wide-angle wind and further support a disk mediated accretion at play for the formation of the central high-mass star.

*Keywords:* ISM: individual objects (G240.31+0.07) – ISM: jets and outflows – stars: formation

## 1. INTRODUCTION

Bipolar molecular outflows, mostly observed in rotational transitions of CO, SiO and some other molecules, are a common phenomenon associated with young stellar objects (YSOs) of all masses (Zhang et al. 2001; Beuther et al. 2002a; Wu et al. 2004, 2005; Maud et al. 2015). It is believed that molecular outflows trace the accretion-powered ejections in sites of low-mass star formation, and they play an important role in the star formation process because of their significant impacts on the surrounding material and the parent cloud. Although molecular outflows have been extensively observed, their driving mechanism remains unknown. Molecular outflows from low-mass YSOs were thought to be produced by the interaction between wide-angle winds and the ambient gas (Shu et al. 1991; Lee et al. 2001), or by jet bow shocks (Raga & Cabrit 1993; Masson & Chernin 1993; Lee et al. 2001). Although the wind-driven model and the jet-driven model can both explain some ob-

served outflow features, none of them are capable of producing all of the observed features of different types of outflows (Lee et al. 2000, 2002). Two-component models with both a highly collimated jet and a wide-angle wind were then developed to establish a unified picture of the observed outflow features (Shu et al. 2000; Banerjee & Pudritz 2006; Pudritz et al. 2006; Shang et al. 2006; Pudritz et al. 2007; Machida et al. 2008).

Massive molecular outflows, which are associated with high-mass YSOs, are less understood than their low-mass counterparts. Due to the rarity and typically large distances, there are few studies toward outflows driven by massive YSOs. Although observations have shown that the morphology and kinematics of some massive outflows are very similar to what is observed for those driven by low-mass YSOs (Shepherd et al. 1998; Beuther et al. 2002b; Qiu et al. 2009; Ren et al. 2011), extremely collimated outflows and circumstellar disks have remained elusive for sources more massive than those equivalent to early B-type stars (Arce et al. 2007). And there is a lack of theoretical work on modeling outflows from high-mass YSOs. Many questions, e.g., how the outflows from massive YSOs are accelerated, how they

differ from low-mass outflows, and how they affect the high-mass star-forming processes, are still unanswered.

Most previous studies of outflows have used low-J rotational transitions of CO (transitions up to  $J_{\text{up}} = 3$ , with upper-state energies  $E_{\text{up}}$  up to 30 K), which are readily excited at low temperatures and can be easily observed by ground-based facilities, to characterize the morphology and kinematics of the relatively cold and extended molecular gas. Due to the Earth's atmosphere, mid-J CO lines (referring to CO  $J = 6-5$  and  $7-6$  throughout this paper, with  $E_{\text{up}}$  up to 150 K), which are less affected by the ambient gas, are not commonly observed. In several studies, mid-J CO transitions have been reported to trace the warm gas ( $>50$  K) in outflows of low-mass and intermediate-mass YSOs (van Kempen et al. 2009a,b; Yıldız et al. 2012; van Kempen et al. 2016). By comparing multi-line CO observations (both low-J and mid-J) with the results of radiative transfer models, the physical properties (temperature, gas density and CO column density) of the outflowing gas could be better constrained (Lefloch et al. 2015).

This paper is a follow-up study of the G240.31+0.07 (hereafter G240) outflow (Qiu et al. 2009). We report the 12-m submillimeter Atacama Pathfinder Experiment Telescope<sup>1</sup> (APEX) observations of G240, an active high-mass star-forming region associated with IRAS 07427-2400 and located at a distance of 5.4 kpc (Choi et al. 2014; Sakai et al. 2015). It harbors an ultracompact HII region and is associated with OH and H<sub>2</sub>O masers (Hughes & MacLeod 1993; Caswell 1997; MacLeod et al. 1998; Migenes et al. 1999; Caswell 2003). Its far-infrared luminosity of  $10^{4.7} L_{\odot}$  is consistent with a spectral type O8.5 zero-age main-sequence star (MacLeod et al. 1998). Kumar et al. (2003) mapped the CO  $J = 3-2$  emission with a  $20''$  beam. From C<sup>18</sup>O  $J = 2-1$  observations, Kumar et al. (2003) found the cloud velocity ( $v_{\text{cloud}}$ ) with respect to the local standard of rest to be  $\sim 67.5 \text{ km s}^{-1}$ . Qiu et al. (2009) presented a detailed high-resolution study of CO  $J = 2-1$  and <sup>13</sup>CO  $J = 2-1$  emissions and detected a bipolar, wide-angle, quasi-parabolic molecular outflow. Li et al. (2013) theoretically interpreted the G240 outflow as a result from interaction between a wide-angle wind and the ambient gas in the form of turbulent entrainment. Recently, Qiu et al. (2014) reported the detection of an hourglass magnetic field aligned within  $20^\circ$  of the outflow axis.

In this paper, we present a CO multi-transition ( $J = 2-1$ ,  $3-2$ ,  $6-5$ , and  $7-6$ ) study toward the G240 outflow. With rotation diagram (RD) and large velocity gradient (LVG) calculations, we estimate the physical parameters of the outflow as functions of gas velocity. We then discuss the results of the analysis.

## 2. OBSERVATIONS

The observations were performed with the 12 m APEX telescope. The APEX CO  $J = 6-5$  and CO  $J = 7-6$  observations were performed in 2010 July with the Carbon Heterodyne Array of the MPIfR (CHAMP+) (Kasemann et al. 2006). The APEX CO (3-2) observations were made in 2011 October using the First Light APEX Submillimeter Heterodyne (FLASH) receiver (Heyminck et al. 2006).

Pointings were checked by comparing these lines with the CO  $J = 2-1$  data adopted from Qiu et al. (2009), and were found to be within  $\sim 7''$  for CO  $J = 3-2$  and within  $\sim 4''$  for CO  $J = 6-5$  and  $J = 7-6$ . The system temperatures were found to be ? at ? GHz. The ? spectrometer was used as the backend with a resolution of ? kHz (?  $\text{km s}^{-1}$ ). The data were smoothed to  $2 \text{ km s}^{-1}$ , then the rms noises in the spectra in the central part of the map are of the order 0.03-0.05 K at 345 GHz, 0.15-0.25 K at 691 GHz and 0.40 - 0.60 K at 809 GHz at the central region of the maps. Noises are higher at the edge of the maps. Beam efficiencies, determined by observations of planets, were 0.65, 0.41 and 0.40 at 345 GHz, 691 GHz and 809 GHz, respectively. The APEX beam sizes are  $\sim 19''$  at 345 GHz,  $\sim 9''$  at 691 GHz and  $\sim 8''$  at 809 GHz. Calibration uncertainties were assumed to be 15 %, 20% and 30% at 345 GHz, 691 GHz and 809 GHz, relatively. These data were complemented with the previously observed combined data from the Submillimeter Array<sup>2</sup> (SMA) and the Caltech Submillimeter Observatory<sup>3</sup> (CSO) 10.4 m telescope in CO  $J = 2-1$  (Qiu et al. 2009). The CO  $J = 2-1$  data has a calibration uncertainty of 10 %, with the rms estimated to be 0.06-0.10 K in  $2 \text{ km s}^{-1}$  channels. Table 1 shows a summary of the line informations.

## 3. RESULTS

### 3.1. CO emission maps

The CO  $J = 3-2$ ,  $6-5$ , and  $7-6$  emissions are detected (with obvious outflow signatures and with peak inten-

<sup>1</sup> The Atacama Pathfinder Experiment Telescope is a collaboration between the Max-Planck-Institut für Radioastronomie, the European Southern Observatory, and the Onsala Space Observatory.

<sup>2</sup> The Submillimeter Array is a joint project between the Smithsonian Astrophysical Observatory and the Academia Sinica Institute of Astronomy and the Astrophysics and is funded by the Smithsonian Institution and the Academia Sinica.

<sup>3</sup> The Caltech Submillimeter Observatory was supported by the NSF grant AST-0229008 and was decommissioned in 2015.

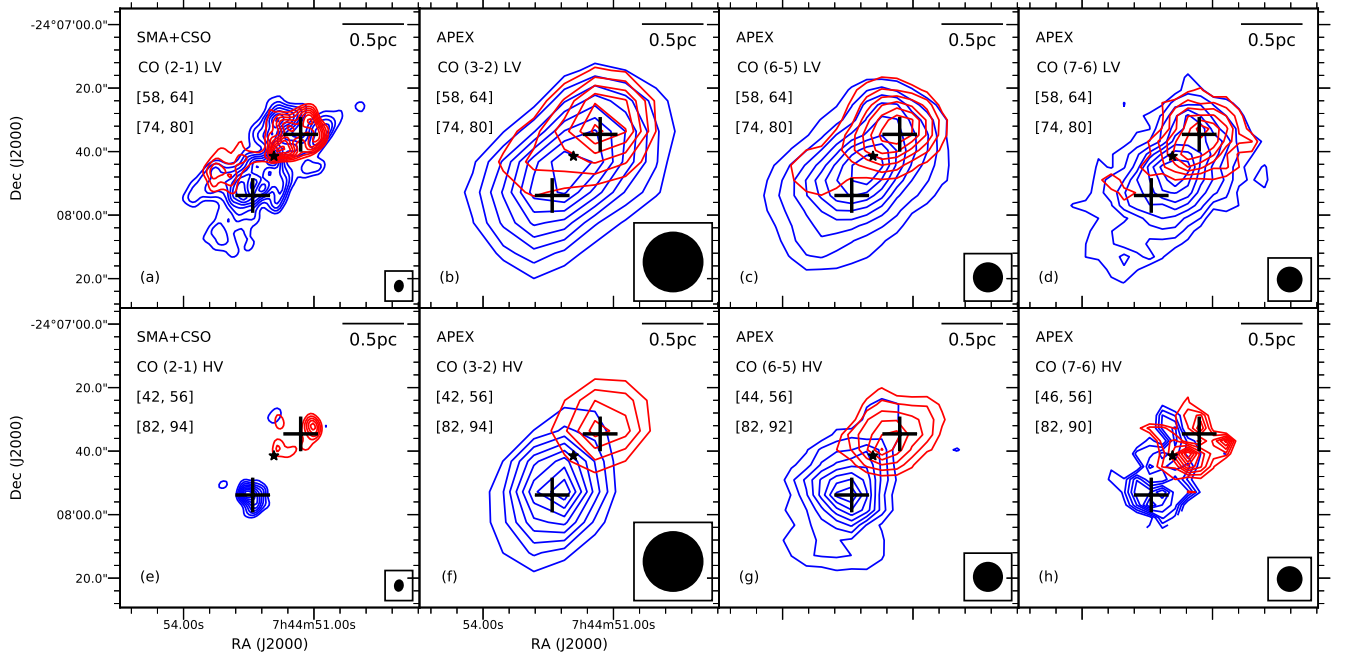


**Figure 1.** (a)-(d) Low-velocity CO  $J = 2-1$ ,  $3-2$ ,  $6-5$ , and  $7-6$  emissions, integrated from 58 to 64  $\text{km s}^{-1}$  for the blueshifted lobe (blue) and from 74 to 80  $\text{km s}^{-1}$  for the redshifted lobe (red); (e)-(f) High-velocity CO  $J = 2-1$  and  $3-2$  emissions, integrated from 42 to 56  $\text{km s}^{-1}$  for the blueshifted lobe (blue) and from 82 to 94  $\text{km s}^{-1}$  for the redshifted lobe (red); (g) High-velocity CO  $J = 6-5$  emission, integrated from 44 to 56  $\text{km s}^{-1}$  for the blueshifted lobe (blue) and from 82 to 92  $\text{km s}^{-1}$  for the redshifted lobe (red) (h) High-velocity CO  $J = 7-6$  emission, integrated from 46 to 56  $\text{km s}^{-1}$  for the blueshifted lobe (blue) and from 82 to 90  $\text{km s}^{-1}$  for the redshifted lobe (red). For (a)-(g), the contour levels start from 20% and continue at steps of 10% of the peak emission. For (h), the contour levels start from 30% and continue at steps of 10% of the peak emission. Edge channels are masked out because of high noise levels. The black star marks the position of a  $\text{H}_2\text{O}$  maser spot which is associated with IRAS 07427-2400 (Sakai et al. 2015). The beam of each observational dataset is shown in the lower right corner of each panel.

**Table 1.** Line informations

| CO line | Frequency | Beam size            | $\sigma_{cal}$ <sup>a</sup> | $\sigma_{rms}$ <sup>b</sup> | $\eta_s$ <sup>c</sup> |
|---------|-----------|----------------------|-----------------------------|-----------------------------|-----------------------|
|         | GHz       | "                    | %                           | K                           |                       |
| 2-1     | 230.5380  | $3.93 \times 3.10^d$ | 10                          | 0.08                        | —                     |
| 3-2     | 345.7960  | 19.16                | 15                          | 0.04                        | 0.65                  |
| 6-5     | 691.4731  | 9.49                 | 20                          | 0.20                        | 0.41                  |
| 7-6     | 806.6518  | 8.12                 | 30                          | 0.50                        | 0.40                  |

<sup>a</sup>Calibration error.

<sup>b</sup>Average rms in 2  $\text{km s}^{-1}$  channels.

<sup>c</sup>Beam efficiency.

<sup>d</sup>Major axis  $\times$  minor axis.

sities greater than  $2 \sigma_{rms}$ ) in velocity ranges from 42 to 94  $\text{km s}^{-1}$ , 44 to 92  $\text{km s}^{-1}$ , and 46 to 90  $\text{km s}^{-1}$ , respectively. Figure 1 shows the integrated low-velocity

(LV) and high-velocity (HV) emissions of the four lines. The velocity ranges chosen to highlight the LV and HV components of the outflowing gas follow those in Qiu et al. (2009), except that the channels with no detections were excluded for the HV component. The morphologies of the bipolar outflow seen in the CO  $J = 3-2$ ,  $6-5$ , and  $7-6$  lines are very similar. Due to the coarser angular resolutions, the wide-angle structure seen in the higher resolution CO  $J = 2-1$  image is not seen in the CO  $J = 3-2$ ,  $6-5$ , and  $7-6$  maps.

### 3.2. Physical conditions of the outflow

The physical condition of the outflow can be constrained by comparing the observed line intensities with the results of statistical-equilibrium calculations. To study the four lines at the same spatial resolution, the CO  $J = 2-1$ ,  $6-5$ , and  $7-6$  maps were reconstructed with the same beam of the CO  $J = 3-2$  map. The rms noise levels are  $\sim 0.004$  K,  $\sim 0.04$  K and  $\sim 0.1$  K for the convolved CO  $J = 2-1$ ,  $6-5$  and  $7-6$  data, respectively. For both lobes of the outflow, the CO line intensities were

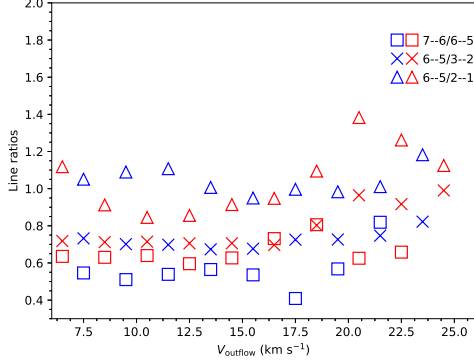


**Figure 2.** Ratios of the main-beam temperatures of different CO lines at different velocities. Blue symbols denote the measurements from the blueshifted lobe, and red symbols the redshifted lobe. The  $V_{\text{outflow}}$  shown here is related to the cloud velocity  $v_{\text{cloud}}$  by the relation:  $V_{\text{outflow}} = |v_{\text{outflow}} - v_{\text{cloud}}|$ , where  $v_{\text{outflow}}$  is the outflow velocity with respect to the local standard of rest.

measured at approximately the peak positions of the HV components of the convolved CO maps (marked as two crosses in every panel of Figure 1), and were then used in the following analysis. Figure 2 shows the ratios of the main-beam temperatures ( $T_{\text{mb}}$ ) of different CO lines as functions of velocity. The CO 7–6/6–5, 6–5/3–2, and 6–5/2–1 ratios are almost constant over a velocity range of  $\sim 5$ – $25 \text{ km s}^{-1}$  with respect to the cloud velocity, with ratio variations of  $< 30\%$ . The typical values of the 7–6/6–5, 6–5/3–2, and 6–5/2–1 ratios are  $\sim 0.6$ ,  $\sim 0.7$ , and  $\sim 1.0$ , respectively. In the analysis, we only used channels of  $\leq 60 \text{ km s}^{-1}$  and  $\geq 74 \text{ km s}^{-1}$  to avoid contaminations from the ambient gas, and we excluded channels of  $< 46 \text{ km s}^{-1}$  or  $> 90 \text{ km s}^{-1}$  because of their low signal-to-noise ratios. Since we didn’t correct the observed line intensities for unknown beam filling factors, the derived CO column density ( $N$ ), gas temperature ( $T$ ), and gas density ( $n$ ) should be considered as beam-averaged values. In the calculation, errors on line intensities took into account both the uncertainties of the flux calibration uncertainty and the rms noise.

We first performed a simple RD analysis (Goldsmith & Langer 1999) to estimate the excitation condition of the outflowing gas under the assumption of local thermal equilibrium (LTE). Considering that the  $^{13}\text{CO } J = 2-1$  emission was only marginally detected or not detected at our considered velocities (Qiu et al. 2009), we assumed the four  $^{12}\text{CO}$  lines to be optically thin. The population of each energy level is given by

$$N_{\text{up}} = \frac{N_{\text{CO}}}{Z} g_{\text{up}} e^{-E_{\text{up}}/kT_{\text{kin}}}, \quad (1)$$

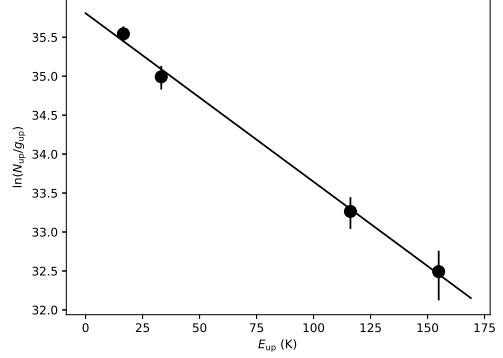


**Figure 3.** A rotation diagram for CO at  $84 \text{ km s}^{-1}$ . The fitted line shows the Boltzmann distribution of the rotational populations. The line represents a rotational temperature of  $48.5 \text{ K}$  and a total column density of  $2.0 \times 10^{15} \text{ cm}^{-2}$ . The black solid circles show the data with error bars.

where  $N_{\text{up}}$  is the column density in the upper state,  $g_{\text{up}}$  the statistical weight of the upper state,  $E_{\text{up}}$  the upper energy level,  $k$  the Boltzmann constant, and  $Z$  is the partition function. The rotation diagram for CO at  $84 \text{ km s}^{-1}$  is shown in Figure 3 as an example. An LTE model at  $48.5 \text{ K}$  could account for the measurements from the four lines. Other velocity channels show similar rotation diagrams.

To better constrain the gas temperature, the density, and the CO column density without assuming LTE and optical thin emission, we then performed radiative transfer calculations of the four lines using the RADEX code, which adopts the LVG approximation (van der Tak et al. 2007). We built a large grid of LVG models by varying the three parameters ( $n$ ,  $T$  and  $N$ ), and obtained the best fitting results by  $\chi^2$  minimization in comparing the observation with the models. With four lines observed and three parameters to constrain, our fitting had one degree of freedom. In Figure 4, the fitting results at  $84 \text{ km s}^{-1}$  are shown. Figure 4(a) and Figure 4(b) show that the gas temperature is well constrained to  $\sim 50 \text{ K}$ . In Figures 4(b) and 4(c), the CO column density is stringently constrained to  $2.2 \times 10^{15} \text{ cm}^{-2}$ . The  $\chi^2$  distribution in Figure 4(a) and 4(c) indicate that in the best LVG models, the gas density is high enough to thermalize the emissions, and thus only lower limits of the gas density could be derived from the  $\chi^2$  minimization. This implies that the LTE assumption adopted by the above RD analysis is valid, and hence we obtain similar gas temperatures and CO column densities from the RD and LVG analyses. Similar  $\chi^2$  distribution patterns were found at other velocities. The reduced  $\chi^2$  ( $\chi^2_{\text{red}}$ ) of the best fitting results varies from 0.10 to 1.72 at different velocities. The representative uncertainty

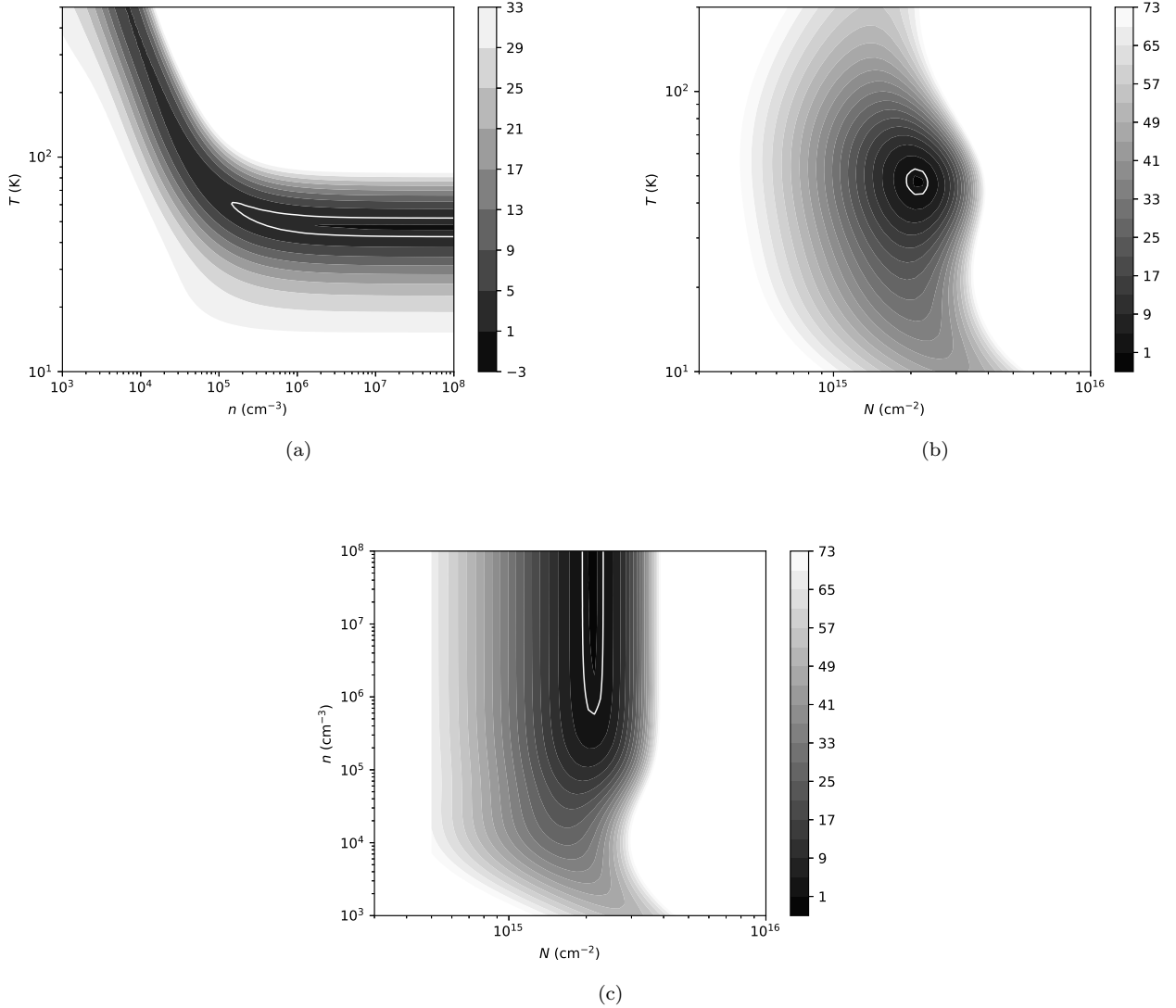


**Figure 4.** (a)-(c) The  $\chi^2$  distribution at  $84 \text{ km s}^{-1}$  in the  $[T, n]$ ,  $[T, N]$  and  $[n, N]$  planes, with the third parameter fixed to the value of the best fitting result at this velocity. The lower limit of gas density is  $1.8 \times 10^5 \text{ cm}^{-3}$ . The best-fit solution is obtained for  $T = 46.1 \text{ K}$  and  $N = 2.2 \times 10^{15} \text{ cm}^{-2}$ . The  $\chi^2_{\text{red}}$  of the best-fit solution is 1.00. The Solid white contours show the  $1\sigma$  confidence levels.

of each parameter is derived from the  $1\sigma$  confidence region in the 3D parameter space at the velocities where  $\chi^2_{\text{red}} \sim 1$ : the relative uncertainty of the CO column density is  $\sim 10\%$ ; the temperature uncertainty is  $\sim 10 \text{ K}$ ; and the gas density is  $> 10^5 \text{ cm}^{-3}$  over the entire velocity range. The modeling results also predict that the four transitions are optically thin in the outflowing gas. Figure A1 shows the comparison of the observed CO intensities with the LVG modeling results in each velocity bin. The best fitting solution can well account for the emission of the four lines.

The variation of the physical conditions of the outflowing gas as a function of velocity is of great interests to

our understanding of the driving mechanism of the outflow. With the RD and LVG analyses we have estimated the gas temperature, density and CO column density at different velocities. Figure 5 shows the temperature-velocity ( $T$ - $V$ ) and CO column density-velocity ( $N$ - $V$ ) relations. In Figure 5(a), the  $T$ - $V$  diagram shows that the emission of the outflow is well accounted for by gas with a temperature of  $\sim 50 \text{ K}$ . The temperature variation of  $< 10 \text{ K}$  is within the expected uncertainties, indicating that the outflowing gas is approximately isothermal. Figure 5(b) shows a clear decreasing trend of CO column density with outflow velocity, with the CO column density in each  $2 \text{ km s}^{-1}$  bin ranging from  $\sim 2 \times 10^{16} \text{ cm}^{-2}$



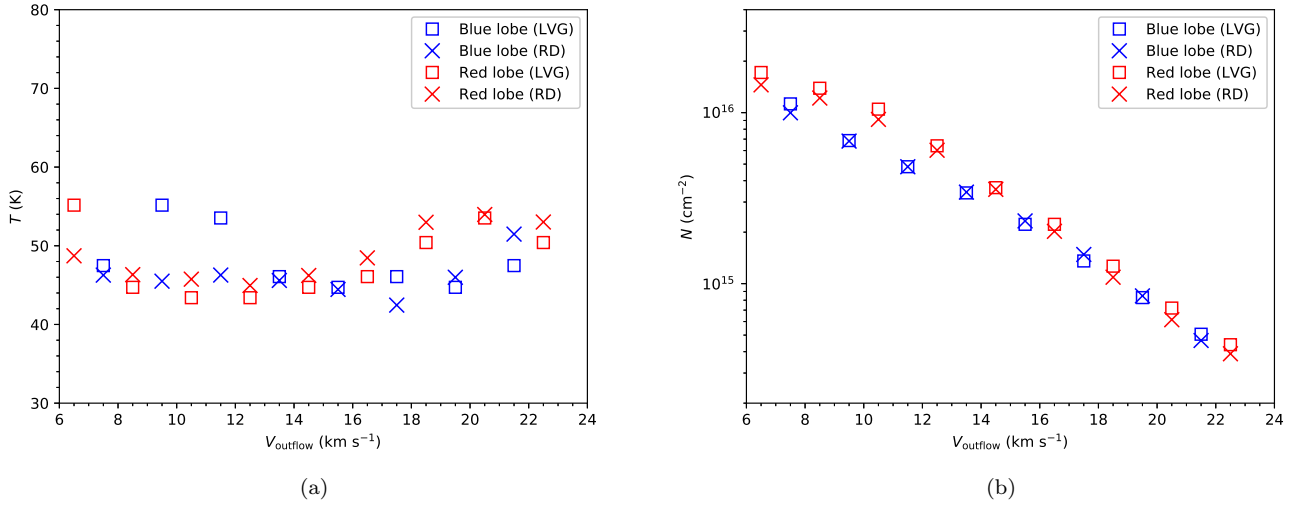


**Figure 5.**  $T$ - $V$  and  $N$ - $V$  diagrams of the G240 outflow, estimated from the RD analysis (blue “x” markers for the blue lobe and red “x” markers for the red lobe) and the LVG analysis (blue open squares for the blue lobe and red open squares for the red lobe).

to  $\sim 4 \times 10^{14}$  cm $^{-2}$  within the outflow velocity range of  $\pm 7$ –22 km s $^{-1}$ . We performed RD and LVG analyses of the CO lines in different positions, and obtained similar  $T$ - $V$  and  $N$ - $V$  relations. Thus, we feel confident that the derived  $T$ - $V$  and  $N$ - $V$  trends are not affected by the systematic bias of position offsets.

#### 4. DISCUSSION

The morphology and kinematics of molecular outflows have been widely studied based on single spectral line observations. However, the physical conditions of the outflow gas are still not well constrained. In particular, how the physical conditions vary with the outflow velocity is poorly understood. To precisely constrain the physical properties of molecular outflows, CO observations across a wide range of energy levels are needed. Previous studies show that CO transitions of  $J_{\text{up}} > 9$  (high- $J$ ) and with  $J_{\text{up}} \leq 9$  should be fitted with different gas components, and that the hotter, denser gas component traced by high- $J$  CO lines only constitutes a small amount of the gas in the molecular outflow (Gomez-Ruiz et al. 2013; Lefloch et al. 2015). Thus, the driven mechanism of the bulk of the molecular outflow is best studied in lines of  $J_{\text{up}} \leq 9$ . Our multi-line analysis with both low- $J$  and mid- $J$  CO line observations have constrained the CO column density and the temperature of the G240 outflow as functions of the outflow velocity, showing a clear example on the physical conditions of a representative well-defined bipolar wide-angle molecular outflow in a  $> 10^4 L_{\odot}$  massive star-forming region (Qiu et al. 2009).

##### 4.1. Temperature

The variation of the outflow temperature with the outflow velocity have been studied only in a handful of sources. van Kempen et al. (2009a) and Yıldız et al. (2012) performed LVG calculations on single-dish CO  $J = 3$ –2 and 6–5 lines, and suggested that there is little or no temperature change within outflow velocity ranges of  $< 10$ –15 km s $^{-1}$  in the outflow associated with low-mass protostars HH46 IRS1 and NGC 1333 IRAS 4A/4B. Considering that van Kempen et al. (2009a) have observed rising CO 3–2/6–5 ratios at more extreme velocities, and that the line wing ratios of CO 3–2/6–5 observed by Yıldız et al. (2012) have relatively large variations, their conclusions of “constant” outflow temperatures are not robust. The temperature of the outflowing gas as a function of velocity in the outflow associated with a high-mass star-forming region was first derived by Su et al. (2012), who performed an LVG analysis on interferometer CO  $J = 2$ –1 and 3–2 observations of the extremely high velocity outflow associated with the high-mass star-forming region G5.89–0.39, and found an increasing temperature with outflow velocity for outflow velocities up to 160 km s $^{-1}$ . Based on the variation of the CO 2–1/1–0 line ratio at a resolution of 32.5'' and assuming LTE, Xie & Qiu (2018) found that the excitation temperature of the outflow in the massive star-forming region IRAS 22506+5944 increases from low ( $\sim 5$  km s $^{-1}$ ) to moderate ( $\sim 8$ –12 km s $^{-1}$ ) velocities, and then decrease at higher velocities ( $< 30$  km s $^{-1}$ ). However, Su et al. (2012) and Xie & Qiu (2018) have only used low- $J$  CO lines with small energy ranges, which are not

sufficient to trace the relatively warm and dense gas. Moreover, all of the above mentioned works have made assumptions about other parameters (e.g., gas density, canonical CO fractional abundance, or velocity gradient) or the equilibrium state (e.g., LTE) of the outflow to infer the  $T$ - $V$  relations from only two CO lines, while these assumptions might not be necessarily valid. Recently, the outflow properties were more precisely determined via multi-line CO studies by Lefloch et al. (2015), who performed an LVG analysis on the outflow cavity ( $<40 \text{ km s}^{-1}$ ) of the intermediate-mass Class 0 protostar Cepheus E-mm and revealed that the outflowing gas traced by CO transitions of  $J_{up} \leq 9$  is nearly isothermal. Our analysis, for the first time, reveals the temperature-velocity relation in a high-mass star-forming region with both low- $J$  and mid- $J$  observations via the LVG calculation. The results show that the G240 outflow is approximately isothermal with a gas temperature of  $\sim 50 \text{ K}$  within an outflow velocity range of  $<23 \text{ km s}^{-1}$ . This isothermal state is similar to the behavior of the outflowing gas (traced by CO transitions of  $J_{up} \leq 9$ ) associated with low-mass and intermediate-mass protostars (Yildız et al. 2012; Lefloch et al. 2015), and the temperature of  $\sim 50 \text{ K}$  is slightly lower than the temperature for outflows of low-mass protostars (van Kempen et al. 2009a; Yıldız et al. 2012) and intermediate-mass protostars (van Kempen et al. 2016). In addition, the derived outflow temperature is warmer than the previously adopted  $\sim 30 \text{ K}$  (Qiu et al. 2009), which indicates that the physical parameters (mass, momentum, energy) of the G240 outflow calculated by Qiu et al. (2009) were underestimated by a factor of 1.32.

#### 4.2. Density

From the LVG analysis, the beam-averaged CO column density is well constrained in each velocity bin, while the constraint for the gas density is loose. Figure 5(b) shows that, from  $\pm 7 \text{ km s}^{-1}$  to  $\pm 22 \text{ km s}^{-1}$  with respect to the cloud velocity, the beam-averaged CO column density decreases by a factor of 50. The decreasing  $N$ - $V$  trend is similar to that of the outflow cavity associated with Cepheus E-mm (Lefloch et al. 2015), and may directly indicate a decrease of the entrained gas with increasing outflow velocity. Since the CO column density degenerates with the beam filling factor in the optically thin case, the observed CO column density could be affected by the beam dilution effect. However, the beam filling factor only decreases by a factor of  $\sim 2.5$  (derived from source sizes of  $\sim 20''$  to  $\sim 10''$ , see Figure 3 of Qiu et al. (2009)) within the outflow velocity range, which could not fully explain the decrease of the observed CO column density with velocity. We argue that

the decrease in CO column density with outflow velocity is due to the change of the gas density. Assuming a constant  $[\text{CO}]/[\text{H}_2]$  abundance ratio, which is adopted by most previous works, the decreasing CO column density indicates a decline of the gas column density with velocity. If the velocity gradient do not vary much, the decreasing gas column density with velocity implies that the gas density decreases with velocity. Taken together, the variations of the beam-averaged CO column density and the beam filling factor suggest that the gas density is  $>10^6 \text{ cm}^{-3}$  at the lowest outflow velocity. This gas density limit is comparable to that in the outflow cavity associated with Cepheus E-mm (Several times of  $10^5 \text{ cm}^{-3}$ ; Lefloch et al. 2015). In summary, our observations indicate that both the CO column density and the gas density decrease with an increasing outflow velocity.

#### 4.3. The origin of the G240 outflow

With high-resolution CO  $J = 2-1$  observations, Qiu et al. (2009) found that the G240 outflow has a well-defined, bipolar, wide-angle, quasi-parabolic morphology and a parabolic position-velocity structure in the northwest redshifted lobe. The kinematic structure and morphology are similar to low-mass wide-angle outflows. However, observations toward low-mass YSOs show that wide-angle low-velocity molecular outflows are usually accompanying with collimated high-velocity atomic/molecular jets: e.g., IRAS 04166+2706 (Santiago-García et al. 2009), L1448-mm (Hirano et al. 2010), and HH 46/47 (Velusamy et al. 2007). But the G240 region shows no signature of a high-velocity jet in infrared, millimeter, and centimeter emissions (Kumar et al. 2002; Qiu et al. 2009; Trinidad 2011). Thus, it is still unclear whether the G240 outflow is driven in a way analogous to that of low-mass outflows or in a different way.

To further investigate the physical conditions and to explore the driven mechanism of the G240 outflow, we presented multi-line analysis of the outflow, and revealed that the temperature of the outflowing gas is relatively constant with outflow velocity, and that the density of the outflow decreases with gas velocity. These trends are in agreement with the estimations of a simple wide-angle wind-driven model, which predict that the outflow is approximately isothermal because of efficient cooling, and that the outflow density decreases with velocity and distance from the driving source as the wind sweeps up the ambient material, which has a density inversely proportional to the square of distance from the source (Shu et al. 1991; Lee et al. 2001). In contrast, the jet-driven bow shock model predicts that the

gas temperature and the density of the outflow increase with velocity and distance from the driving source due to shock heating and compressing (Lee et al. 2001), which are different from our results. The none-detection of a high-velocity jet in the G240 region also rules out the jet-driven bow shock model. Although most existing wind-driven outflow models can only explain typical parameters of outflows driven by low-mass YSOs, recent theoretical results provide evidence that massive outflows can also be driven by wide-angle disk winds (Matsushita et al. 2018). Thus, our analyses results support the scenario that the G240 outflow is mainly driven/entrained by a wide-angle wind, which itself may resemble the accretion-driven wide-angle winds (X-wind or disk winds: Shang et al. 2006; Pudritz et al. 2006) associated with low-mass YSOs. We further suggest that disk-mediated accretion may exist in the formation of high-mass stars up to late-O types.

## 5. SUMMARY

Using the APEX CO J = 3–2, 6–5 and 7–6 observations and the complementary CO J = 2–1 data, we have presented the first CO multi-transition study toward the molecular outflow of the high-mass star-forming region G240. The parsec-sized, bipolar, and high velocity outflow is clearly revealed by the CO J = 3–2, 6–5 and

7–6 emissions. For both lobes, the outflow is approximately isothermal with a temperature of  $\sim 50$  K. The CO column density of the outflow decreases with gas velocity, which indicates that the gas density decreases with outflow velocity if the CO abundance and velocity gradient remain relatively constant. The isothermal state and the decreasing gas density indicate that the wind-driven/entrainment is the dominant driving mechanism of the G240 outflow. This finding further suggests that disk-accretion can be responsible for the formation of high-mass stars more massive than early B-type stars.

We thank the APEX staff for carrying out the observations, and Yu Cheng for helpful discussions on RADEX modelling. Keping Qiu acknowledges support from the National Natural Science Foundation of China (Grant Nos. 11473011 and 11590781). This research made use of APLpy, an open-source plotting package for Python (Robitaille & Bressert 2012), Astropy, a community-developed core Python package for Astronomy (Astropy Collaboration et al. 2013), and Matplotlib, a Python 2D plotting library for Python (Hunter 2007).

*Facility:* Atacama Pathfinder Experiment (APEX).

*Software:* APLpy (Robitaille & Bressert 2012), Astropy (Astropy Collaboration et al. 2013), Matplotlib (Hunter 2007).

## REFERENCES

- Arce, H. G., Shepherd, D., Gueth, F., et al. 2007, *Protostars and Planets V*, 245
- Astropy Collaboration, Robitaille, T. P., Tollerud, E. J., et al. 2013, *A&A*, 558, A33
- Banerjee, R., & Pudritz, R. E. 2006, *ApJ*, 641, 949
- Beuther, H., Schilke, P., Sridharan, T. K., et al. 2002, *A&A*, 383, 892
- Beuther, H., Schilke, P., Gueth, F., et al. 2002, *A&A*, 387, 931
- Caswell, J. L. 1997, *MNRAS*, 289, 203
- Caswell, J. L. 2003, *MNRAS*, 341, 551
- Choi, Y. K., Hachisuka, K., Reid, M. J., et al. 2014, *ApJ*, 790, 99
- Frank, A., Ray, T. P., Cabrit, S., et al. 2014, *Protostars and Planets VI*, 451
- Goicoechea, J. R., Cernicharo, J., Karska, A., et al. 2012, *A&A*, 548, A77
- Goldsmith, P. F., & Langer, W. D. 1999, *ApJ*, 517, 209
- Gomez-Ruiz, A. I., Wyrowski, F., Gusdorf, A., et al. 2013, *A&A*, 555, A8
- Heyminck, S., Kasemann, C., Güsten, R., de Lange, G., & Graf, U. U. 2006, *A&A*, 454, L21
- Hirano, N., Ho, P. P. T., Liu, S.-Y., et al. 2010, *ApJ*, 717, 58
- Hirota, T., Machida, M. N., Matsushita, Y., et al. 2017, *Nature Astronomy*, 1, 0146
- Hughes, V. A., & MacLeod, G. C. 1993, *AJ*, 105, 1495
- Hunter, J. D. 2007, *Computing in Science and Engineering*, 9, 90
- Kasemann, C., Güsten, R., Heyminck, S., et al. 2006, *Proc. SPIE*, 6275, 62750N
- Kumar, M. S. N., Bachiller, R., & Davis, C. J. 2002, *ApJ*, 576, 313
- Kumar, M. S. N., Fernandes, A. J. L., Hunter, T. R., Davis, C. J., & Kurtz, S. 2003, *A&A*, 412, 175
- Lee, C.-F., Mundy, L. G., Reipurth, B., Ostriker, E. C., & Stone, J. M. 2000, *ApJ*, 542, 925
- Lee, C.-F., Stone, J. M., Ostriker, E. C., & Mundy, L. G. 2001, *ApJ*, 557, 429
- Lee, C.-F., Mundy, L. G., Stone, J. M., & Ostriker, E. C. 2002, *ApJ*, 576, 294
- Lefloch, B., Gusdorf, A., Codella, C., et al. 2015, *A&A*, 581, A4
- Li, G.-X., Qiu, K., Wyrowski, F., & Menten, K. 2013, *A&A*, 559, A23



- Machida, M. N., Inutsuka, S.-i., & Matsumoto, T. 2008, *ApJ*, 676, 1088-1108
- MacLeod, G. C., Scalise, E., Jr., Saedt, S., Galt, J. A., & Gaylard, M. J. 1998, *AJ*, 116, 1897
- Masson, C. R., & Chernin, L. M. 1993, *ApJ*, 414, 230
- Matsushita, Y., Sakurai, Y., Hosokawa, T., & Machida, M. N. 2018, *MNRAS*, 475, 391
- Maud, L. T., Moore, T. J. T., Lumsden, S. L., et al. 2015, *MNRAS*, 453, 645
- Migenes, V., Horiuchi, S., Slysh, V. I., et al. 1999, *ApJS*, 123, 487
- Pudritz, R. E., Rogers, C. S., & Ouyed, R. 2006, *MNRAS*, 365, 1131
- Pudritz, R. E., Ouyed, R., Fendt, C., & Brandenburg, A. 2007, *Protostars and Planets V*, 277
- Qiu, K., Zhang, Q., Wu, J., & Chen, H.-R. 2009, *ApJ*, 696, 66
- Qiu, K., Zhang, Q., Menten, K. M., et al. 2014, *ApJL*, 794, L18
- Raga, A., & Cabrit, S. 1993, *A&A*, 278, 267
- Ren, J. Z., Liu, T., Wu, Y., & Li, L. 2011, *MNRAS*, 415, L49
- Robitaille, T., & Bressert, E. 2012, *Astrophysics Source Code Library*, ascl:1208.017
- Sakai, N., Nakanishi, H., Matsuo, M., et al. 2015, *PASJ*, 67, 69
- Santiago-García, J., Tafalla, M., Johnstone, D., & Bachiller, R. 2009, *A&A*, 495, 169
- Shang, H., Allen, A., Li, Z.-Y., et al. 2006, *ApJ*, 649, 845
- Shepherd, D. S., Watson, A. M., Sargent, A. I., & Churchwell, E. 1998, *ApJ*, 507, 861
- Shu, F. H., Ruden, S. P., Lada, C. J., & Lizano, S. 1991, *ApJL*, 370, L31
- Shu, F. H., Najita, J. R., Shang, H., & Li, Z.-Y. 2000, *Protostars and Planets IV*, 789
- Su, Y.-N., Liu, S.-Y., Chen, H.-R., & Tang, Y.-W. 2012, *ApJL*, 744, L26
- Trinidad, M. A. 2011, *AJ*, 142, 147
- van der Tak, F. F. S., Black, J. H., Schöier, F. L., Jansen, D. J., & van Dishoeck, E. F. 2007, *A&A*, 468, 627
- van Kempen, T. A., van Dishoeck, E. F., Güsten, R., et al. 2009, *A&A*, 501, 633
- van Kempen, T. A., van Dishoeck, E. F., Güsten, R., et al. 2009, *A&A*, 507, 1425
- van Kempen, T. A., Hogerheijde, M. R., van Dishoeck, E. F., et al. 2016, *A&A*, 587, A17
- Velusamy, T., Langer, W. D., & Marsh, K. A. 2007, *ApJL*, 668, L159
- Wu, Y., Wei, Y., Zhao, M., et al. 2004, *A&A*, 426, 503
- Wu, Y., Zhang, Q., Chen, H., et al. 2005, *AJ*, 129, 330
- Xie, Z.-Q., & Qiu, K.-P. 2018, *Research in Astronomy and Astrophysics*, 18, 019
- Yıldız, U. A., Kristensen, L. E., van Dishoeck, E. F., et al. 2012, *A&A*, 542, A86
- Zhang, Q., Hunter, T. R., Brand, J., et al. 2001, *ApJL*, 552, L167

## APPENDIX

## A. SPECTRAL LINE FLUX DISTRIBUTIONS

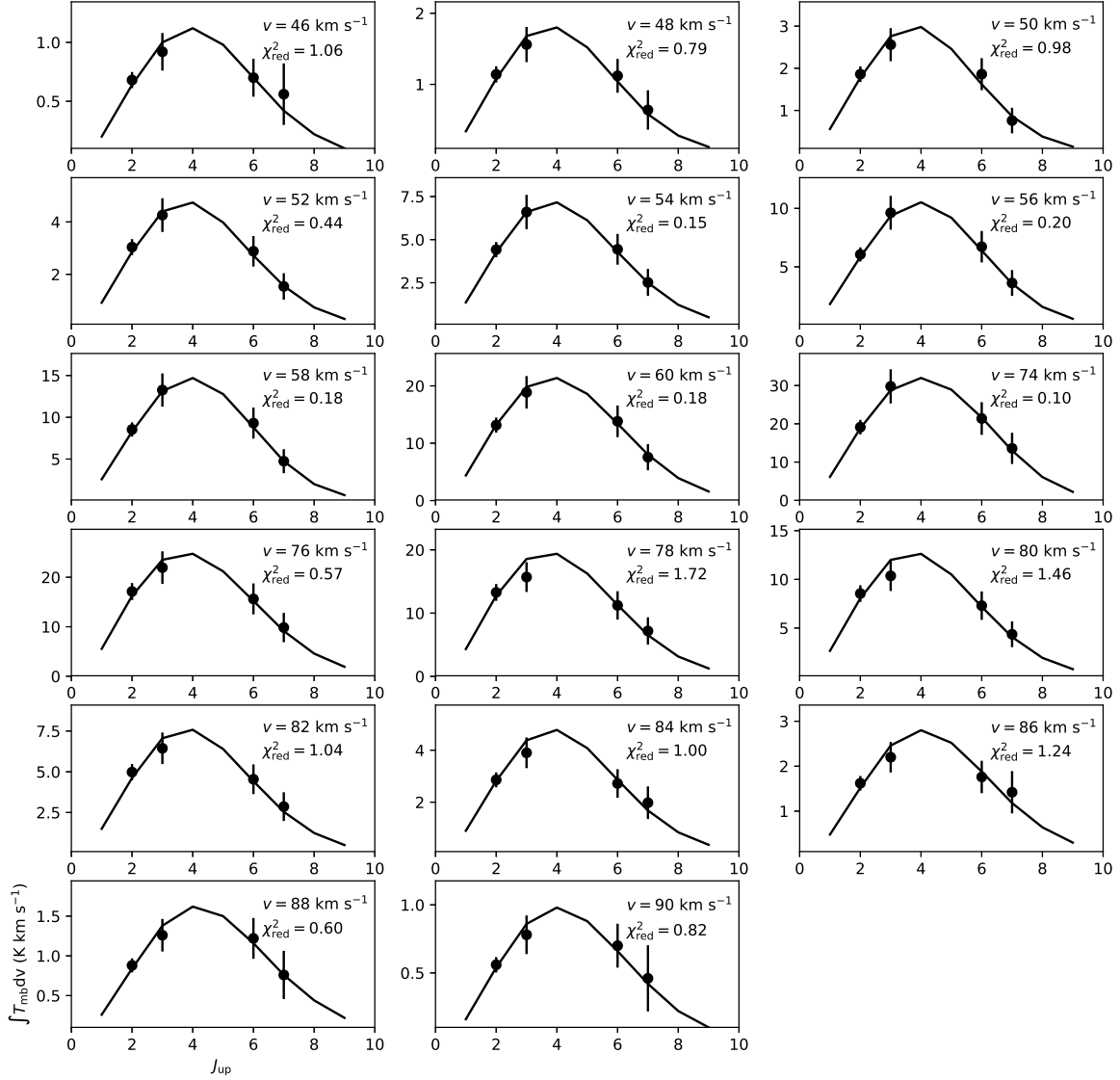


**Figure A1.** Observed line fluxes compared with the LVG computations in each 2 km s $^{-1}$  bin. The black solid circles show the observed data with error bars. The black solid lines refer to the best fits. The  $\chi^2_{\text{red}}$  of the best fitting results and the outflow velocities are shown in each panel.